Spectral energy scattering and targeted energy transfer in phononic lattices with local vibroimpact nonlinearities

Joshua R. Tempelman ⬤, Alexander F. Vakakis ⬤, and Kathryn H. Matlack ⬤
Department of Mechanical Science and Engineering, University of Illinois at Urbana-Champaign,
1206 West Green Street, Urbana, Illinois 61801, USA

We propose a method for manipulating wave propagation in phononic lattices by employing local vibroimpact (VI) nonlinearities to *scatter* energy across the underlying linear band structure of the lattice, and *transfer* energy from lower to higher optical bands. First, a one-dimensional, two-band phononic lattice with embedded VI unit cells is computationally studied to demonstrate that energy is scattered in the wave number domain, and this nonlinear scattering mechanism depends on the energy of the propagating wave. Next, a four-band lattice is studied with a similar technique to demonstrate the concept of nonresonant interband targeted energy transfer (IBTET) and to establish analogous scaling relations with respect to energy. Both phononic lattices are shown to exhibit a maximum energy transfer at moderate input energies, followed by a power-law decay of relative energy transfer either to the wave number domain or between bands on input energy. Last, the nonlinear normal modes (NNMs) of a reduced order model (ROM) of a VI unit cell are computed with the method of numerical continuation to provide a physical interpretation of the IBTET scaling with respect to energy. We show that the slope of the ROM's frequency-energy evolution for 1:1 resonance matches well with IBTET scaling in the full lattice. Moreover, the phase-space trajectories of the NNM solutions elucidate how the power-law scaling is related to the nonlinear dynamics of the VI unit cell.

I. INTRODUCTION

Periodicity has been leveraged to control acoustic and elastic energy propagation in linear time-invariant (LTI) phononic metamaterials [1–3]. Such systems are typically designed on a unit cell level whereby the application of the Bloch theorem allows one to *engineer* a linear band structure which can enable or augment specified wave phenomena with diverse applications such as lensing [4], vibration isolation [5–7], wave steering [8], and topological insulation [9–11]. For LTI phononic systems, a propagating wave remains stationary on a prescribed subset of its band structure, and is invariant to amplitude (or energy) as the dynamics are completely described by the superposition principle [3]. However, it is often desirable to predictively tune wave propagation in phononic materials in a nonstationary or amplitude-dependent fashion. To this end, one must either manipulate the underlying band structure altogether by utilizing external forces or nonlinearity [3,12], or find methods to modify the distribution of (or, equivalently, passively manage) energy across a fixed underlying band structure.

Whereas active band manipulation has been achieved by introducing (active) multiphysics fields, e.g., electromagnetic, magnetic, or thermal fields [13–18], nonlinear mechanisms considered here, such as nonlinear mechanical coupling, offer the key advantage of being passive and tunable (self-adaptive) to energy, frequency, and wave number content [12,19]. For instance, the effective dispersion relations of granular chains with Hertzian contact laws are tunable by locally linearizing about various precompression states [20–22]. Moreover, passive nonlinear mechanisms possess intrinsic frequency-amplitude dependencies which are predictable by Bloch-wave perturbation analysis in the low-energy regime [23] or by the nonlinear normal modes (NNMs) of the finite lattice in the high-energy regime [24–26].

The use of nonlinear attachments in acoustic waveguides (either bulk or periodic) has demonstrated unprecedented properties in acoustical systems [27]. For instance, a small mass connected to a resonator chain by an essential (non-linearizable) stiffness nonlinearity has been shown to induce interesting nonlinear dynamics when interacting with traveling waves [28], and can even be tuned to arrest incident pules [29]. Moreover, by incorporating hierarchical mass scales and asymmetry, similar systems have achieved acoustic nonreciprocity [30–32]. These effects have been extended for systems with *local* nonlinear gates that enable effective diode-type features in both continuous waveguides [33] and discrete oscillator chains [34,35], and similar concepts have been recently leveraged for mechanical wave filtering in metamaterials with interfaces [36,37].

Herein, we aim to develop passive mechanisms for redistributing propagating energy using *localized* nonlinearities to *transfer* energy across the underlying band structure of a phononic lattice. In the absence of external actions, this requires a nonlinear mechanism with the capacity to transfer energy form one region of band structure to another. Such a mechanism is fundamental to achieving nonlinear energy exchanges, which are most commonly described in terms of phase matching, internal resonances, and resonance captures [38,39]. These nonlinear resonant phenomena have led to the concept of targeted energy transfer (TET) [40]. Among its many applications, TET has previously been

utilized to transfer energy between donor and receptor locations in nonlinear lattices [41]. Recently, TET has been used to design passive nonlinear energy control using local attachments called *nonlinear energy sinks* (NESs) [40]. NESs are local mechanisms that alter the global dynamics of a primary linear structure to which they are attached to achieve TET, with typical applications in vibration mitigation [42–56].

Traditional NES-based TET relies on resonance capture of the NES dynamics to a resonance manifold, and thus traditional TET is intrinsically suited for systems with smooth nonlinearities and periodic excitations [39]. However, theoretical and numerical support has recently been extended to systems with nonstationary dynamics [57] and systems with nonsmooth nonlinearities such as idealized vibroimpact (VI) laws [58–60]. Recent work has introduced the concept of *nonresonant* TET energy exchanges in a directly forced primary linear structure by using VI nonlinearity to redistribute modal energy within its modal space, termed *intermodal targeted energy transfer* (IMTET) [61–63]. Unlike resonant TET, IMTET *scatters* energy across the underlying linear modal basis in a low-to-high-frequency fashion.

To date, nonresonant energy scattering concepts have not been extended to periodic phononic metamaterials from a wave propagation perspective. The most notable differences between modal and periodic acoustical systems are the timescales which describe the dynamics of nonlinear oscillators considered. While both modal and acoustic systems oscillate at fast timescales governed by the eigenfrequencies, the first employs a modal basis to describe stationary vibrations (and is suitable for systems of finite extent whose dynamics are governed by relatively slow timescales, i.e., slow flow dynamics [40]), while the latter focuses on acoustics and relies on a continuous band structure to describe propagating waves (and, hence, applies to unbounded and/or large-scale systems with timescales determined by group velocity and wave-packet bandwidth). Hence, several natural questions arise when considering nonresonant TET phenomena in a phononic material: Namely, to what extent can the linear wave propagation be *scattered* in the wave number domain across a dispersion branch, and to what capacity can energy be irreversibly *transferred* from one band to another by use of localized VI nonlinearities? These desired phenomena are notably distinct from previous studies of TET in lattice systems [27–35,41]. This paper addresses these questions with extensive computational probing, postprocessing techniques, and physics-based reasoning of the resulting nonlinear acoustic phenomena.

We begin by studying the effects of VI nonlinearity in a two-band phononic lattice of diatomic resonators by simulation and numerical postprocessing. For this, we focus on the energy scattered across the frequency-wave number (spectral) domain of the single optical band of this lattice as a function of the number of local VI unit cells and as a function of the incident wave energy growth. Next, we consider a four-band phononic lattice, which has one acoustic and three optical bands over a relatively broad frequency-wave number range. This band structure, coupled with the strong VI nonlinearities, allows for low-to-high-frequency energy generation of the impacts, as well as TET across bands. This brings about the

nonlinear acoustic phenomenon of *interband targeted energy transfer* (IBTET).

Accordingly, the organization of this paper is as follows. Section II provides a system description of the unit cell of the two-band phononic lattice, a computational framework for studying spectral scattering within the single optical band induced by the VIs, and quantification of the spectral disorder generated by the VIs with respect to energy. Section III extends the study to a four-band phononic lattice and presents a method for transferring energy from lower to higher optical bands via VIs, together with relationships between these transfers and the total system energy. Section IV presents a two-degree-of-freedom (2DOF) reduced order model (ROM) which is studied from the perspective of NNM analysis in order to provide a physics-based understanding of the results of Secs. II and III, and relates the nonlinear dynamics of the ROM to the IBTET occurring in the lattice. Last, Sec. V offers concluding remarks and some suggestions for further extension of this work.

II. SPECTRAL ENERGY SCATTERING

We begin by studying a one-dimensional (1D) phononic lattice in the form of a diatomic resonator chain and embed VI contact laws in select (local) resonators while preserving the global linear structure of the lattice. The system is computationally explored by performing numerical simulations with wave-packet excitations over an array of excitation amplitudes and wave numbers. The resulting data sets were postprocessed in the spatial-temporal domain to uncover the underlying trends of energy scattering in the wave number domain as the excitation level (input energy) changes.

A. System description and simulations

We consider a linear diatomic lattice constructed by the periodic tessellation of 1D unit cells in the x direction [Fig. 1(a)]. Each unit cell is composed of a host mass and internal resonator, which, depending on the existence (absence) of rigid barriers, may (may not) experience vibroimpacts [Figs. 1(b) and 1(c)]. The corresponding equations of motion for the *infinite* phononic lattice are

$$m_1 \ddot{u}_1^k = k_1\left(u_1^{k-1} + u_1^{k+1} - 2u_1^k\right) + k_2\left(u_2^k - u_1^k\right),$$
$$m_2 \ddot{u}_2^k = k_2\left(u_1^k - u_2^k\right). \tag{1}$$

Substituting a Bloch-wave solution into Eq. (1) yields a lower-frequency acoustic band and higher-frequency optical band to describe propagation in the lattice.

We consider six different finite lattice configurations, each corresponding to a unique arrangement of VI unit cells embedded in the linear lattice with the number of VIs ranging between 1 and 20 [Fig. 1(d)]. These configurations ensured that the VI interactions remained relatively localized in space with respect to the entire lattice, while also offering insight regarding the dependency of the energy scattering on the number of VI interactions the wave may undergo. We fix $m_1 = 0.01$ kg, $m_2 = 8m_1$, and $k_1 = k_2 = 90$ kN/m unless otherwise stated. Excitation is provided to the left boundary in the form of a windowed harmonic function, $F(t) = W(t)\sin(\Omega t)$,
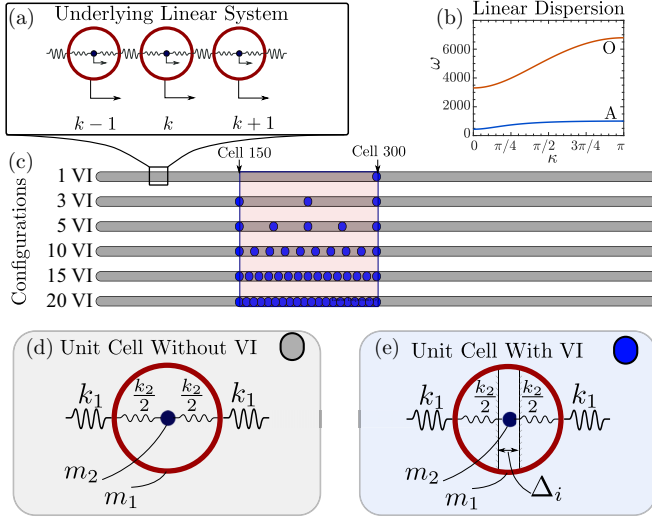
FIG. 1. The linear phononic lattice composed of coupled (host) masses with embedded internal resonators which may or may not undergo vibroimpacts: (a) the primary linear periodic system and (b) the underlying linear dispersion relation showing the acoustic (A) and optical (O) bands. (c) Schematics of finite lattice configurations which are predominately composed of (d) the linear phononic lattice primitive unit cells with (e) nonlinear VI cells embedded at select locations in the lattice.

where $W(t) = A[H(t) - H(t - \frac{2\pi N_c}{\Omega})][1 - \cos(\frac{\Omega t}{N_c})]$ is a windowing function, $H(t)$ the Heaviside function, A the forcing amplitude, N_c the number of cycles in the window, and Ω the center frequency of excitation. The forces induced by the local nonlinear VIs are described by

$$F_{\mathrm{NL}}(w_k) = k_c[(w_k - \Delta_k)_+^n - (-w_k - \Delta_k)_+^n]g(\dot{w}_k), \quad (2)$$

where $w_k(t) = u_2^k(t) - u_1^k(t)$, $n = 3/2$ unless otherwise stated, Δ_k is the clearance of the kth VI in the lattice, and $k_c = \frac{2E_{\mathrm{VI}}\sqrt{R_{\mathrm{VI}}}}{3(1-\nu^2)}$ the stiffness parameter for Hertzian contacts, with $E_{\mathrm{VI}} = 200$ MPa, $R_{\mathrm{VI}} = 0.005$ m, and $\nu = 0.3$ being the modulus, radius, and Poisson ratio of the VI, respectively. The notation $(\ )_+$ indicates that only positive arguments are to be considered. We consider an inelastic dissipation function based on the work-energy principal [64], $g(\dot{w}_k) = (1 - \frac{3(1-r)}{2\dot{w}_k^-}\dot{w}_k)$, where $\dot{w}_k^-$ is the velocity $\dot{w}_k$ immediately before impact and r the coefficient of restitution which is set to $r = 0.7$ to emulate steel-to-steel contact [63]; this roughly equates to an equivalent linear viscous damping constant of $c_{2+} = 5.5 \times 10^{-4} k_2$. Note that Eq. (2) does not modify the underlying linear band structure of the extended lattice and the VIs only affect the propagating waves when $w_k > \Delta_k$ at a given unit cell.

Numerical simulations were performed for center frequencies corresponding to wave number $\kappa = 5\pi/9$. Excitation frequencies were chosen based on the optical band dispersion to ensure relative out-of-phase motion between the resonator and impactor and thus excite the VIs, and the VI clearances were nominally set to range between 0.0002 and 0.0001 m with a logarithmic dependence on position from the leading VI unit cell to account for the momentum loss of the wave as it passes successively through VI cells based on numerical
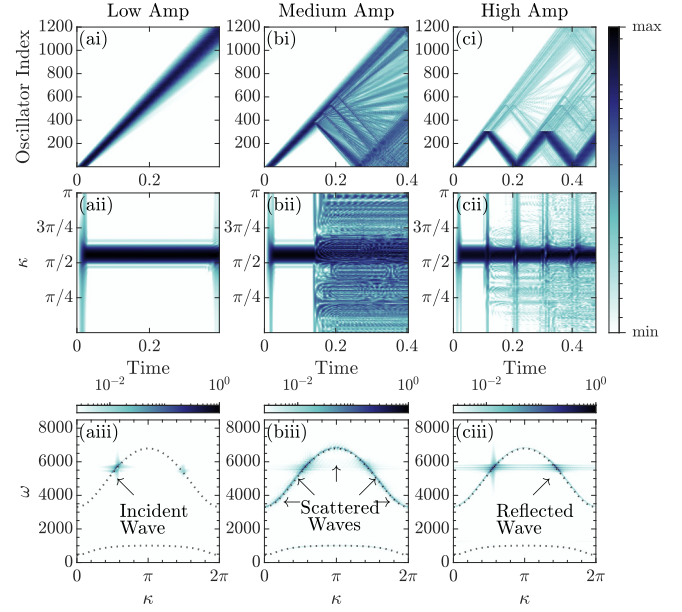

FIG. 2. Simulation results for a five-VI configuration at excitation wave number $k^\star = 5\pi/9$ (in the optical band of the linear lattice) with columns corresponding to (a) low-, (b) medium-, and (c) high-amplitude excitations. For each amplitude, the rows depict (i) the spatiotemporal evolution of the kinetic energy of the propagating wave, (ii) the temporal variation of the wave number distribution in the lattice, and (iii) the numerically computed dispersion computed using the entirety of the simulation with a gray dashed line superimposed to depict the analytical dispersion of the infinite liner lattice

probing of the lattice response at various forcing levels. Within this framework, an ensemble of simulation data was constructed for 25 logarithmically increasing forcing amplitudes for each configuration in Fig. 1.

B. Influence of VIs on wave propagation

In this section, we focus on a narrow subset of three simulations conducted at low, medium, and high forcing amplitudes in order to build intuition on the postprocessing analysis and to establish qualitative dependence of the frequency-wave number distribution on system energy. Quantitative results across all simulations will be given subsequently.

Figure 2 depicts the results for a representative simulation with a five-VI configuration (cf. Fig. 1) for low, medium, and high forcing amplitude (equivalently low-, medium-, and high-energy simulations) corresponding to $A = 0.1$, 1, and 10 N, respectively. The resulting energy measures are computed directly by considering only the kinetic energies of the oscillator. At low amplitude, the acoustics are entirely linear as the wave does not create deflections greater than the VI clearance [Fig. 2(ai)]. The interactions of the VI mechanisms come about in the medium- and high-amplitude simulations, whereby the energy of the propagating wave scatters profoundly in the space-time domain [Figs. 2(bi) and 2(ci)].

To understand the energy scattering in terms of frequency and wave number content, we utilize a set of signal processing procedures that are briefly detailed in Appendix A. Figures 2(aii), 2(bii), and 2(cii) depict the wave number spectrum across the lattice computed over progressions of time

snapshots for each simulation, which was recovered by performing Fourier analysis in the spatial domain over successive time iterations. It is clear from Figs. 2(aii)–2(cii) that the wave number distribution in linear (low-amplitude) simulations does not change after the excitation ends, as expected for a LTI system. In contrast, new wave numbers emerge for medium and high excitation amplitudes. However, for the case of high energy level, the wave number generation is not nearly as pronounced compared to medium energy level, indicating that the wave reflections of Fig. 2(ci) do not generate substantial wave number components beyond that of the incident wave.

Taking the Fourier transformation across both time and space provides the numerically resolved dispersion $\mathcal{D}(\kappa, \omega) = \mathcal{F}^{x,t}\{\mathbf{u}(x, t)\}$ which is given in Figs. 2(aiii)–2(ciii). Figure 2(aiii) may serve as a reference since no VIs engage in the low-amplitude simulations, where only a small region of the optical branch is energetic, corresponding directly to the excitation spectrum. In the nonlinear regimes, the energy scattering over ω-κ is much more profound for medium-energy cases, corroborating the trends established by rows (i) and (ii) of Fig. 2. Note that the spectral content generated by scattering in Fig. 2(biii) remains bound to the underlying linear dispersion relation; this indicates that the VIs "redistribute" (scatter) wave energy across the dispersion relation of the underlying linear lattice in a nonresonant fashion, rather than modify the dispersion altogether. Hence, this nonresonant scattering mechanism yields the same effect for transient wave propagation to that studied in modal dynamics [63].

To visualize the propagation of the wave specific to different partitions of the optical band, and thus confirm that wave propagation at new wave numbers occurs due to VI interactions, customized filter banks were constructed to segment spectral content in the wave number domain. Namely, we follow a similar continuous wavelet transform approach to [65] and partition wavelet-transformed simulation data into 12 wave number partitions. The spatial wavelet-transformed data at a time t, denoted as $X(\kappa, x)|_t$, were multiplied by a masking filter corresponding to the jth partition of the optical band to deliver the binned quantity $\mathcal{K}_j(x, \kappa)$. The propagation in each frequency bin $\mathcal{K}_1$–$\mathcal{K}_{12}$ was then computed as the collection of inverse wavelet transformations of binned wavelet data over time. The kinetic energy can be computed for each spatial-spectral partition with litter error (see Appendix A), which cannot be achieved directly in the frequency domain due to the mass dependency of the kinetic energy. More importantly, as discussed below, the described numerical partition of the optical band enables us to study in detail the transmission of wave energy at different wave number bands and, hence, can offer insight into the nonlinear physics of the scattering of the incident wave at the VI sites.

Figure 3 depicts the results of the wave number partitioning scheme. The propagation of energy across each wave number partition is given by Figs. 3(ai)–(axii) and plotted to the same color scale with respect to kinetic energy. The wave initiates in $\mathcal{K}_7$ and $\mathcal{K}_8$, which are both energetic at the onset of propagation. However, midway through the lattice, the energy begins to propagate through all partitions, and this is clear indication that the VI nonlinearity generates wave number content not native to the incident wave. Figure 3(b) shows the amplitude dependence of the scattering by superimposing the
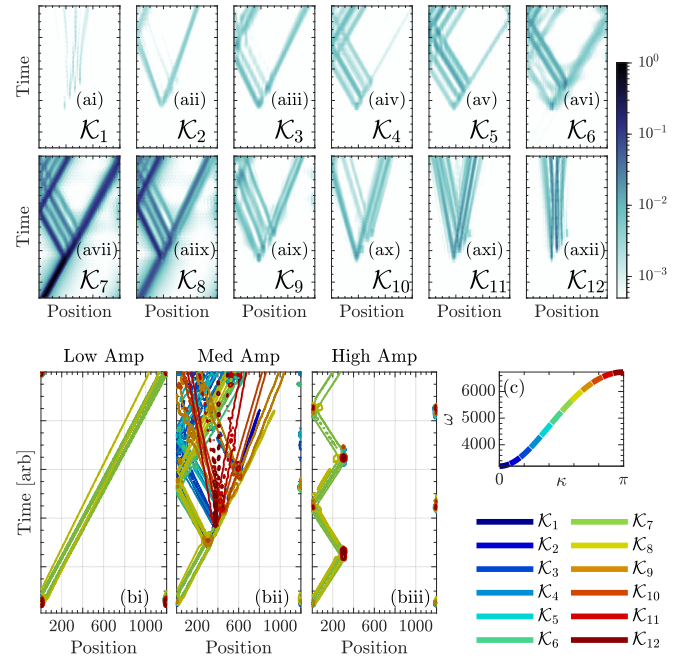

FIG. 3. Propagation of wave energy at different wave number bands: (a) the kinetic energy versus time at each wave number partition for a mid-energy simulation with panels (i)–(vii) plotted to the same color scale to compare relative energies; (b) superimposition of wave propagation at each wave number partition depicted by contours for (i) low-, (ii) medium-, and (iii) high-energy simulation; and (c) the optical band of the linear lattice plotted with corresponding colors to the wave number-based energy contours of (b).

propagation in each wave number band for low-, medium-, and high-profile wave numbers, from which it is apparent again that wave number generation is far more potent at medium-amplitude simulations than for high ones.

C. Quantifying wave number spectrum disorder

Having established, in a qualitative sense, that the VIs generate new wave numbers in an amplitude-dependent fashion (cf. Figs. 2 and 3), we now seek to quantify the spectral scattering and establish empirical relationships with respect to amplitude. To this end, we consider the spectral entropy, which is the extension of classical Shannon entropy to the frequency domain [66], to quantify signal complexity in terms of frequency content. We consider the wave number entropy generated over space at a given time snapshot as

$$H(x) = -\sum_{\kappa} P(x, \kappa) \log_2 P(x, \kappa), \tag{3}$$

where $P(x, \kappa)$ is the space-dependent probability distribution over wave number computed with the space-frequency power spectrogram. Computing $P(x, \kappa)$ over time snapshots, t_j, delivers a matrix of entropy versus time, $\mathcal{H}(x, t)$, capturing the time evolution of wave number entropy of the propagating wave for each simulation.

We compute a statistical summary of the wave number entropy by considering the elements of $\mathcal{H}(x, t)$ for time intervals after the incident wave has already reached the first VI unit cell at $t = \hat{t}$. Figure 4 depicts the average entropy quantity normalized between 0.01 and 1 with respect to forcing ampli-
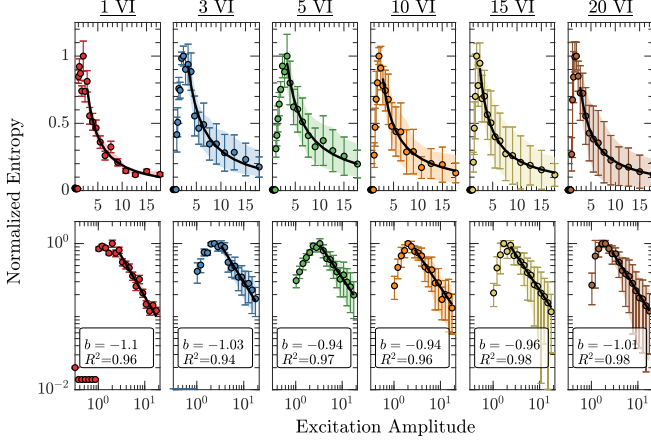
FIG. 4. Mean spectral entropy in the lattice with VIs for system configurations ranging from 1 to 20 VIs (see Fig. 1) over an array of excitation amplitudes logarithmically spaced from 0.1 to 20: Top and bottom plots are for the same data with the bottom plots depicting the log-log scaling; a fitted power law is denoted as a thick black line, and the adjusted R-squared value is listed for each configuration in the bottom plots.
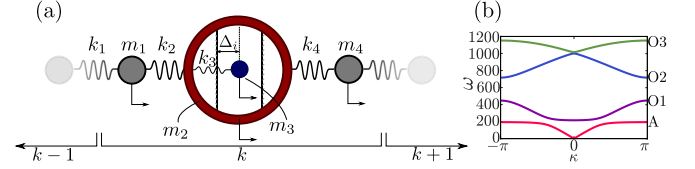

FIG. 5. Increasing the bands of the lattice: (a) schematic of the unit cell and (b) the corresponding dispersion diagram for parameters $\lambda = 0.1$ and $\eta = 0.5$ showing the acoustic band (A) and optical bands 1–3 (O1–O3).

tude for all configurations depicted in Fig. 1. To this effect, we are capturing the *relative* scattering of wave numbers as compared to an *optimal* excitation amplitude for a given VI configuration. For low-amplitude (linear) simulations, the entropy remains nearly zero as the only variation in the wave number comes from the intrinsic dispersive characteristics of the underlying linear lattice (i.e., with inactive VIs). However, once the VIs are engaged at medium and high excitation levels, the entropy rises to a maximum before rapidly falling again with respect to forcing amplitude. Figure 4 reveals that after the maximum entropy is reached, the remainder of the data fit remarkably well with a power law, with adjusted R-squared coefficients above 0.95 being recovered for the majority of configurations studied. The power coefficients b for the law $y = ax^b$ are reported by insets in each panel of Fig. 4 showing that the decay rate has a 1:1 proportion to energy with $b \approx -1$, and that this trend is ubiquitous among each considered configuration (i.e., 1 to 20 VI oscillators). Error bars in Fig. 4 measure the standard deviation of entropy across the spatial extent of the lattice which corresponds to the spatial uniformity of the scattering. Hence, the larger error bounds at high excitation amplitudes indicate that novel wave number components are localized rather than distributed (or propagated) throughout the spatial extent of the lattice, and this is in direct agreement with the qualitative results of Figs. 2 and 3.

III. INTERBAND TARGETED ENERGY TRANSFERS

With Sec. II establishing that the VI nonlinearities can scatter energy about the optical band of a diatomic lattice, we now seek to induce VI-enabled targeted energy across different bands. This can be considered the acoustics equivalent to the IMTET mechanism established for modal dynamics [61]. Hence, this section demonstrates interband targeted energy transfers (IBTET) by showcasing irreversible transfer of energy from a lower optical band to a higher one. Moreover,

we demonstrate this phenomenon for multiple classes of VI contact laws by introducing a nonlinear VI law to be studied alongside the Hertzian model of Sec. II. This demonstrates that the subsequent results are not particular to the Hertzian contact law utilized in Sec. II and thus achievable by a broader design space of phononic wave guides. Achieving IBTET requires additional optical bands above the first optical band, since a spectral feature of VIs is the low-to-high-frequency energy transfers [63]. To maintain the simplicity of one dimension, we proceed with a four-DOF model of the unit cell, offering two additional bands to transfer energy towards.

A. The four-band lattice

The four-band model emulates closely the resonator model of Fig. 1 with the main difference being two masses added in series in between resonators as shown in Fig. 5(a). The equations of motion for a unit cell of the *infinite* four-band phononic lattice read

$$
\begin{aligned}
& m_1 \ddot{u}_1^k + k_4\big(u_1^k - u_4^{k-1}\big) + k_1\big(u_1^k - u_2^k\big) = 0, \\
& m_2 \ddot{u}_2^k + k_2\big(u_2^k - u_1^k\big) + k_3\big(u_2^k - u_3^k\big) \\
& \qquad + k_4\big(u_2^k - u_4^k\big) + f_{\mathrm{NL}}(w^k) = 0, \\
& m_3 \ddot{u}_3^k + k_3\big(u_3^k - u_2^k\big) - f_{\mathrm{NL}}(w^k) = 0, \\
& m_4 \ddot{u}_4^k + k_1\big(u_4^k - u_1^{k+1}\big) + k_4\big(u_4^k - u_2^k\big) = 0. \quad (4)
\end{aligned}
$$

To maximize the potential for IBTET, the parameters of system (4) were selected to ensure that (i) sufficient out-of-phase motion was achieved on the second band (which is selected as the excitation band), (ii) the excitation band corresponds to high group velocities to minimize linear dispersive effects in the simulation, and (iii) the higher bands possess adequate bandwidth to receive the low-to-high-frequency energy redistribution caused by the VI interactions [63], which is equivalent to maximizing their average group velocity over the Irreducible Brillouin Zone. System (4) is parametrized by η and λ which relate the mass and stiffness of the resonator cell to the nominal parameters of $m_1 = m_4 = m = 0.005$ kg and $k_1 = k_4 = k = 2 \times 10^4$ N/m by $m_2 = m(1 - \eta)$, $m_3 = m\eta$, and $k_3 = k\lambda$ while we fix $k_2 = 10^4$ N/m. We confine the design space to $0.1 < \lambda < 1$ and $0.1 < \eta < 1$, and recover $\lambda = 0.1$ and $\eta = 0.5$ (see the Supplemental Material [67]), which results in the band structure shown in Fig. 5(b).

To simulate the system, a finite lattice of 300 unit cells (1200 DOF) was constructed. Accordingly, we consider only a five-VI lattice configuration [as depicted in Fig. 1(d)] herein and refer the reader to the Supplemental Material [67] for
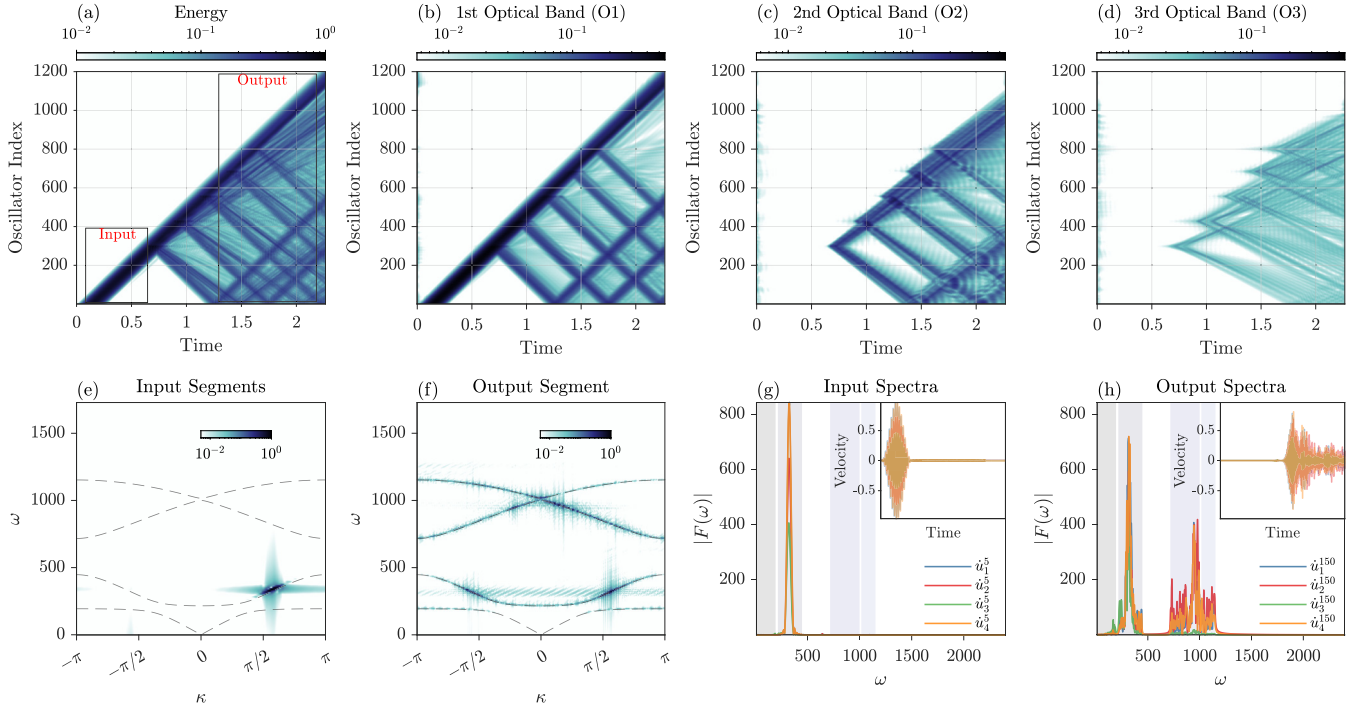
FIG. 6. IBTET in the four-band lattice with five VI sites: (a) evolution of the propagating wave energy; [(b)–(d)] propagation of the wave energy corresponding to each band of the lattice based on the numerically recovered dispersion of the full simulation; [(e), (f)] dispersion of the input and output segments [labeled in (a)] demonstrating the targeted energy transfer to the higher bands; [(g), (h)] Fourier spectra corresponding to the velocity of the four unit cell DOF selected before (fifth unit cell) and after (150th unit cell) VI engagement, with the four bandpass regions depicted with shading and insets depicting the corresponding velocity-time histories.

the results of a one-VI lattice configuration. Simulations were performed similarly to Sec. II with excitation provided by a windowed tone burst. An input signal of 30 periods was considered, and the excitation frequency is selected based on the maximum group velocity of the optical band. Simulations were performed for 50 selections of the excitation amplitude between 1 and 10^4 N.

We employ the same Hertzian contact law described by Eq. (2) for $n = 3/2$, and also a bilinear contact law which takes the same form as Eq. (2) but for $n = 1$. This is performed to ensure that the subsequent results are not particular to nonlinear Hertzian contact laws but are rather a product of the contact nonlinearity. For the four-band system considered, the contact stiffness parameters (k_c) were computed based on $E = 100$ MPa, $\nu = 0.3$, and $R_{VI} = 0.005$ m, and the clearances are now varied between $10^{-2.65}$ and $10^{-2.75}$ m.

B. Low-to-high-band targeted energy transfer

Figure 6 depicts an example of a wave propagating through the four-band system with five Hertzian VIs engaged. Energy clearly cascades from the main wave packet as it propagates through the lattice [Fig. 6(a)], similar to the diatomic chain (Fig. 2). Computing the numerical dispersion at the beginning and end of the simulation clearly shows that energy in fact transfers from the lowest optical band to the higher two optical bands [Figs. 6(f) and 6(g)]. This is further confirmed by Figs. 6(h) and 6(i), which show the difference in the temporal frequency of the wave at the start versus end of the lattice and hence the low-to-high-frequency tar-

geted transfer of energy from the second band to the higher bands.

Energy transfer between bands can be quantified by first converting the numerically measured data into the ω-κ domain with the two-dimensional (2D) Fourier transformation. Thereafter, the 2D spectrum is partitioned band by band and also into band-gap regions. For each partition, the remainder of the spectrum is zero-padded before the inverse Fourier transformation returns the spectral content into the spatiotemporal domain for that specific partition. This results in the propagation depicted in Figs. 6(b)–6(e), where it can be seen that the content of the upper bands indeed corresponds to propagating waves generated by the VIs, and thereafter kinetic energy calculations over each band can be conveniently performed.

Figure 7 depicts the results of the IBTET analysis over the ranges of forcing amplitudes considered for both Hertzian and bilinear VI laws. The log-log plots depict a very similar trend to what was observed in Sec. II: a sudden spike in energy transfer once the amplitude is sufficient enough to engage the VI, and a sudden decline in energy transfer as the excitation amplitudes rise thereafter. This decline in IBTET continues until a minimum is reached which is defined by the relative energy obtained by the higher bands for a completely linear system. This ≈0.01% lower bound of the total system energy is explainable by the fact that the excitation is a Gaussian distribution in the frequency domain which invariably provides trace amounts of energy to the higher bands.

The same trends in IBTET are recovered for both Hertzian and bilinear contacts, indicating that the nature of the contact
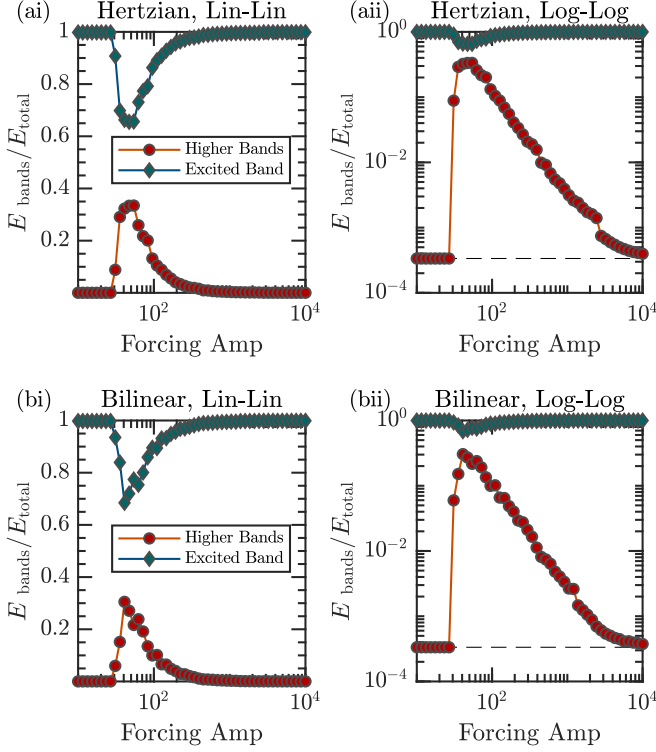
FIG. 7. The portion of input energy transferred to the upper two optical bands versus forcing amplitude of the incident wave for (a) Hertzian VIs and (b) bilinear VIs in (i) linear-linear and (ii) log-log scales.

law does not play a critical role in the energy transfer, but rather the discontinuous potential is the driving mechanism for the energy exchanges. This is further verified in Figs. 7(aii) and 7(bii), which show that the maximum IBTET is on the same order for both the Hertzian and bilinear VIs (30–35 %) which confirms that (i) an appreciable level of IBTET is achievable and (ii) this phenomenon is general across various VI designs.

IV. PHYSICAL INTERPRETATION OF IBTET MECHANISM

We now seek to relate the trends established in Secs. II and III to physics-informed arguments in order to offer physical insight into IBTET in a consistent and comprehensive way. We do so by studying the nonlinear normal modes (NNMs) of a reduced order model (ROM) constructed to emulate the VI unit cells. NNMs have proven a useful tool for interpreting the responses of nonlinear dynamical systems and their passive tunability with respect to energy through either analytical or computational tools [68–71]. The uses and interpretations of NNMs are quite extensive; however, a direct and intelligible way of interpreting the evolution of the system's dynamics with respect to energy is with the frequency energy plot (FEP) of a given dynamical system and its bifurcating branches [68]. Such methodology has been employed already for understanding the dynamical evolution of VI systems of various forms [72–74].
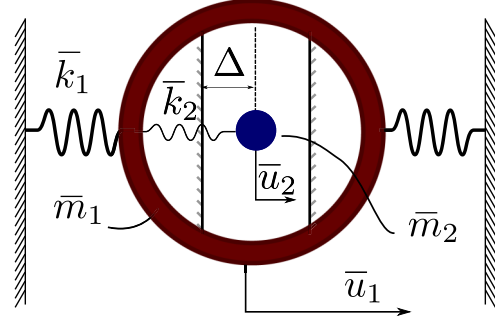

FIG. 8. A 2DOF model emulating a VI resonator cell.

A. Reduced order model

We consider a 2DOF ROM that emulates the individual VI resonators embedded within the four-band lattice of Sec. III. Figure 8 provides a schematic of the ROM whereby the parameters $\bar{k}_1 = k = 2 \times 10^4$ N/m, $\bar{k}_2 = 2 \times 10^3$ N/m, and $\bar{m}_2 = \bar{m}_2 = 0.0025$ kg parametrize the set of equations

$$\bar{m}_1 \ddot{\bar{u}}_1 + \bar{k}_1 \bar{u}_1 + k_2(\bar{u}_1 - \bar{u}_2) + f_{\text{NL}}(\bar{w}) = 0,$$
$$\bar{m}_2 \ddot{\bar{u}}_2 + \bar{k}_2(\bar{u}_2 - \bar{u}_1) - f_{\text{NL}}(\bar{w}) = 0, \tag{5}$$

where an overbar denotes that the variable is associated with the ROM and not the full phononic lattice. The nonlinear force in Eqs. (5) is considered in both Hertzian and bilinear forms with a contact stiffness and clearance of $10^{-2.75}$ m.

We assume that the connecting stiffness between masses in the lattice is distributed between the two mass elements. Thus, the grounding stiffness on the left and right boundaries of the ROM's outer mass is approximated to be one-half of the coupling stiffness of the full phononic lattice. Moreover, the most critical component of the ROM is the internal stiffness and nonlinear VI component, which matches identically to the VI cells considered in Sec. III. Hence, the ROM provides reasonable resemblance to the VI cells in the full lattice system, allowing it to capture the trends of the full system with surprisingly good accuracy, as we will show.

B. Nonlinear normal modes as a measure of nonlinearity

The energy dependencies of Figs. 4 and 7 make continuation of NNM branches a natural approach since it provides an overview of the dynamics across energy scales. To this end, we apply the NNM continuation scheme described in [71] to our ROM with minor numerical modifications (see Appendix B). A condensed description of this procedure is given, and the reader is directed to [71] for full algorithmic details. The state form of system (5) is $\dot{\mathbf{z}} = \mathbf{g}(\mathbf{z})$, where $\mathbf{g}(\mathbf{z})$ is a nonlinear function of the state variables. A periodic orbit (or NNM) will satisfy the two-point boundary value problem defined by the *shooting function*, $\mathbf{H}(\mathbf{z}_{\mathbf{p}_0}, T) = \mathbf{z}(\mathbf{z}_{\mathbf{p}_0}, T) - \mathbf{z}_{\mathbf{p}_0} = \mathbf{0}$. A phase condition of zero initial velocities is employed to ensure unique NNM solutions, and with this Newton's method returns the first NNM during the *shooting* stage. After the shooting stage, a pseudoarclength predictor-corrector routine traces out the NNM branch in the $(2n + 1)$-dimensional parameter space, where n is the number of degrees of freedom of the ROM. This is a critical step
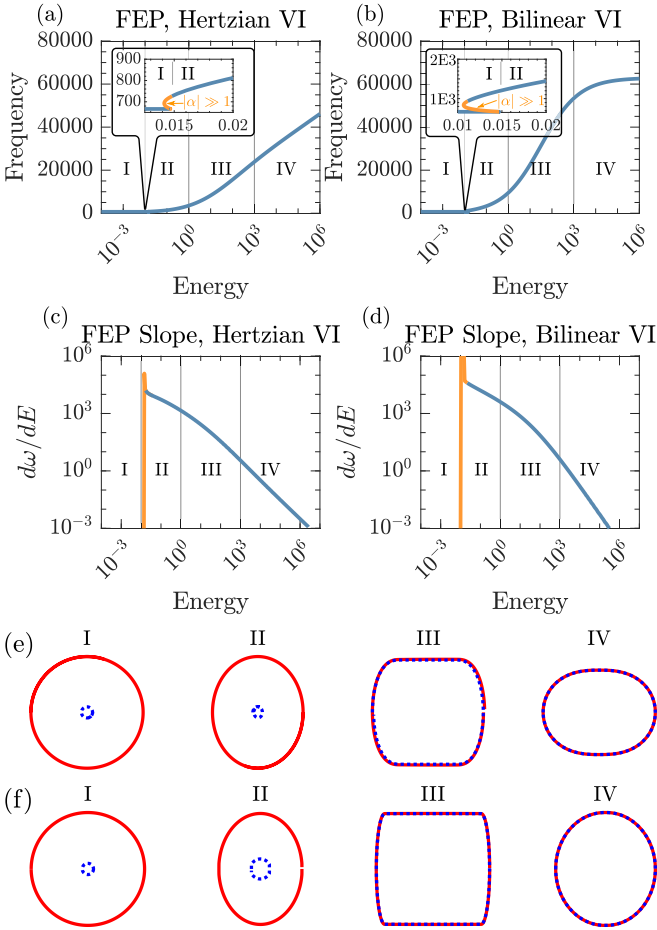
FIG. 9. The FEPs of the ROMs with (a) Hertzian and (b) bilinear nonlinearity with insets zooming in on the transition from region I to region II with instability denoted by orange for regions with Floquet multipliers $|\alpha| \gg 1$; [(c), (d)] slopes of the FEPs of (a) and (b) with respect to energy; [(e), (f)] corresponding phase trajectories of the NNMs for (a) and (b), respectively, for regions I, II, III, and IV of the FEPs.

for resolving the NNMs of the VI system since the NNM branches may have turning points that a standard Newton-Raphson algorithm cannot solve.

The result of numerical continuation is a *frequency energy plot*, which describes the evolution of the NNM branch for 1:1 resonance (the "backbone" branches) in the frequency-energy space. Figure 9 depicts the FEPs computed for the system described by Eqs. (5) for both Hertzian and bilinear contact laws. It is interesting to emphasize that the degree (strength) of nonlinearity of the ROM can be qualitatively interpreted by the slope of a given NNM branch [72]. The steeper the slope of the branch is, the more sensitive the frequency-amplitude dependency of the NNM becomes, and the more intense is the nonlinearity in the ROM when it responds on that NNM.

The FEP results reveal similar trends for both Hertzian and bilinear VI ROMS, possessing four dynamical regions labeled I–IV in Fig. 9 which describe the transition between two distinct smooth limiting systems. The corresponding phase trajectories of the periodic orbits in each region are given in Figs. 9(e) and 9(f) for Hertzian and bilinear models, respectively. In the low-energy region I, the VIs do not engage,

and the dynamics are completely linear; this is confirmed by zero slope of the FEP and can be regarded as the low-energy limiting system. In region II, there is a grazing of the VI contacts, causing a sudden change in the dynamics and a rapid increase of FEP slope; this marks the critical energy required to engage the VIs. Here, the corresponding NNM branch folds back on itself towards lower energies before transitioning towards higher energies, with this effect being more prevalent in the bilinear model (the Hertzian nonlinearity being less prominent in the small-deflection-amplitude limit). This fold in the NNM branch yields a small neighborhood of energies where the FEP slope is theoretically infinite, and these energies correspond to the maxima of Figs. 9(c) and 9(d), indicating that the transition from region I to region II represents a transition where the dynamics are most sensitive to nonlinear effects. Despite the apparent smoothness of Figs. 9(eII) and 9(fII) the volatile VI-grazing dynamics in region II are unstable as determined by the maximum magnitude of the NNM Floquet multipliers, α, which greatly exceed unity for the energy regions depicted by orange lines in Fig. 9. Hence, the solutions corresponding to maximum FEP slopes are not physically realizable.

After grazing, the FEP gradually increases in frequency towards region III. Region III is characterized by strong VI oscillations which is apparent by the boxlike phase trajectories indicating nonsmooth temporal dynamics. Here, the linear dynamics of $\bar{k}_1$ are negligible and the VI dynamics dominate; however, the VI forces only interact with the oscillator for localized time windows during an oscillation cycle (hence the nonsmooth phase portrait). It is in region III that the slopes of the FEPs decrease in a power-law-like fashion as the ROM asymptotically reaches the limiting region IV. This asymptotic approach corresponds to the power-law decline of the FEP slopes of Figs. 9(c) and 9(d). The physical interpretation of this result is as follows. As the energy increases, so too does the frequency and the indentation depth of the VI. As a result, the VI forces exist for relatively longer durations during the periodic oscillation as energy grows. This corresponds to a transition from the boxlike nonsmooth VI phase trajectories marked by sudden changes in kinetic and potential energies, to the limiting smooth dynamics of region IV. Region IV is characterized by in-phase dynamics dominated by the contact stiffness; this can be regarded as the high-energy limiting system. In this region, the clearance is negligible and the VI contacts behave as an extremely stiff elastic spring. Hence, the dynamics of the ROM with Hertzian contacts approaches a smoothly nonlinear system with a 3/2 nonlinear coupling, whereas the dynamics of the bilinear ROM approaches a linear system at high energy, as is confirmed by the phase portraits of Figs. 9(eIV) and 9(fIV). Moreover, for the bilinear system, the FEP clearly levels off as the high-energy (almost) linear limiting behavior is reached.

C. Relating the dynamics of the ROM to the acoustics of the lattice

The evolution of the FEP slope with respect to energy of the ROM [Figs. 9(b) and 9(c)] possess a remarkable similarity to trends of nonlinear IBTET in the full phononic lattice (Fig. 7). The two measures can be related to one another by
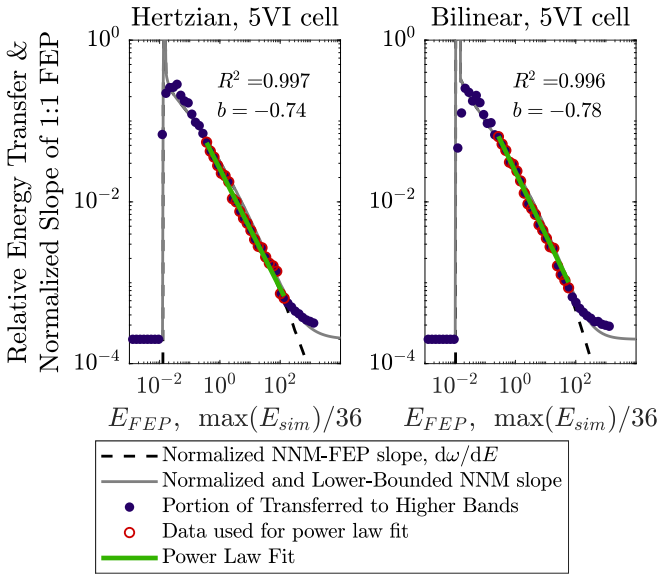
FIG. 10. The relative interband energy transfer, with the normalized slope from the ROM-FEP superimposed for (a) Hertzian and (b) bilinear contact models; the dashed lines depict the normalized FEP slopes, the gray lines depict the normalized FEP slopes lower bounded by the initial (linear) energy of the higher bands, and green lines depict a power-law fit to red dots, with the adjusted R-squared value shown with the inset.

replotting the energy transfers of Fig. 7 with respect to system energy (to match the energy-dependent nature of the FEP) and superimposing the FEP slopes to compare similarities in their evolution with energy. To do this requires a normalization, as the maximum and minimum values of the FEP slope can be arbitrarily large or small, whereas the relative energy of the upper optical bands is lower bounded by the amount provided by the excitation source (from the Fourier uncertainty principal), and upper bounded by unity (since the energy in the upper bands cannot exceed the total energy of the system). Moreover, the wave propagation in the 1200-DOF phononic lattice carries the energy of 30 cycles of the windowed excitation, whereas the FEP energy is parametrized by the periodic orbits of the 2DOF ROM. Thus, the energy of the finite lattice must be normalized in order to be commensurate with the energy of the ROM used to generated the FEP. These normalizations are performed as follows. The FEP slope is divided by a scalar to quantitatively align with the relative energy transfer so that a direct comparison can be made with respect to decay rate versus energy. A scalar quantity defined by the low bound of IBTET (dashed lines of Fig. 7) is then added to the FEP slope to account for the lower threshold of the energy transfer in the VI lattice. The energy of the finite lattice is normalized so that the *initiation energy*, that is, the energy required to engage the first VI site encountered by the propagating wave front, aligns with the transition between regions I and II of the FEP. These normalizations preserve the slopes of both quantities since scalar multiplication results only in translations for logarithmic scaling. Hence, the amplitude-normalized FEP slopes can be directly compared to energy-normalized IBTET when superimposed. Figure 10 displays the described superposition where a remarkable agreement is found between the

trends in the slope of the FEP of the ROM and the energy transfer between bands in the lattice. Hence, the underlying FEP of the ROM, along with the evolution of the dynamical regimes of Fig. 9, clearly has a direct implication of the IBTET in the lattice. Moreover, by fitting a slope to the measured energy transfer versus normalized system energy for data points falling in region III, a near-perfect power law is recovered as indicated by the adjusted R-squared values close to 1 (see Fig. 10). Finally, these results are in agreement with the trends observed for spectral spreading within the optical band of the two-band system considered in Sec. II, indicating that the same physical arguments developed in Sec. IV B can be used to interpret the trends of Sec. II as well. Hence, the numerical results presented for the finite lattices can be understood in terms of the underlying nonlinear dynamics of the ROM as it transitions from a limiting low-energy linear system to a highly nonlinear VI system, and then asymptotically approaching a smooth high-energy limiting system. With this, a predictive tool is presented to assess the capacity for IBTET in full phononic systems based on the simplified VI ROMs which, being of low dimensionality, are much more amenable to analysis compared to the extended nonlinear lattices considered herein.

V. CONCLUSIONS

In this work, we have investigated the effect of local VI nonlinearities on the propagation of traveling waves in 1D phononic lattices. Specifically, first a diatomic two-band lattice was numerically studied over a wide range of forcing amplitudes and embedded VI configurations (Sec. II). It was demonstrated that spectral energy transfer in the optical band of this lattice is most profound for moderate excitation amplitudes, and decreases in effectiveness as the energy rises (Fig. 2). This was quantified using the spatial-spectral entropy (or wave number entropy) for various systems which all followed very closely to power-law decays with respect to excitation amplitude after the peak value was reached (Fig. 4). Attention then turned to interband targeted energy transfer (IBTET) in a four-band system (Sec. III). Simulations were carried out over a range of excitation amplitudes, and numerical postprocessing of wave scattering demonstrated that IBTET is indeed possible. Moreover, this phenomenon was proven effective for both Hertzian and bilinear VIs, and the trends in IBTET with respect to excitation amplitude followed closely those observed for spectral energy transfer in the two-band lattice (Fig. 7).

To provide some physical insight into the effect of the VIs on the acoustics of the lattice, a 2D ROM was constructed based on the unit VI cell. The underlying FEP of the ROM was computed for the NNM family of 1:1 resonance branches which revealed four dynamic regimes that the ROM assumes with respect to energy, namely, a limiting linear low-energy region, a grazing region characterized by the initiation of VI interactions, a VI-oscillator regime with nonsmooth temporal dynamics, and an *effectively* linear or smoothly nonlinear limiting high-energy regime, depending on the contact law (Hertzian or bilinear). This, in turn, produced a frequency-energy slope that directly scales to the trends of IBTET in the lattice with respect to system energy, providing the physical

interpretation of the spectral scattering of Secs. II and III. Moreover, the FEP presents a means for accurately predicting energy transfer capacity of the full phononic lattice based on the low-dimensional ROM.

Although this work focused primarily on fundamental understanding of the physics at play, the implications and potential for future developments are rather extensive. The low-to-high-energy transfers directly correspond to a reduction in magnitude, since the energy must be preserved in the frequency transfer. Moreover, the evolution of the VI dynamics with respect to energy corresponds to an effective filter that can greatly alter transmissibility of incident waves (cf. Fig. 2). These attributes alone make VI-based methods attractive for wave transmission tuning (or tailoring) with respect to amplitude. Moreover, while we have targeted low-to-high-energy transfers between bands, future works could explore the potential for targeting specific bands and specific subregions of bands of phononic lattices by optimizing the distribution and parameters of local VIs in lattices through methods such as genetic programming or machine learning.

APPENDIX A: DETAILS ON SIGNAL PROCESSING PROCEDURES

1. Continuous wavelet transformation

In this section, we provide a brief discussion of the wavelet transformation algorithm employed in this work in order to clarify the mathematical details pertinent for performing the wavelet-based wave number partition analysis of Sec. II (cf. Fig. 3). A similar discourse may be found in [65]. The continuous wavelet transformation (CWT) is traditionally used as a time-frequency analysis tool by transforming the signal from the time domain to the time-frequency domain. To the same effect, one can consider the space-wave number domain. For 1D systems the standard definition of the CWT with respect to the spatial variable x is

$$X(\kappa, x) = \sqrt{\frac{\kappa}{\kappa_c}} \int_{-\infty}^{\infty} u(\xi) \psi^* \left(\kappa \frac{\xi - x}{\kappa_c} \right) d\xi, \quad \text{(A1)}$$

where $\psi^*(\xi)$ is the complex conjugate of the mother wavelet function and κ_c the center frequency,

$$\kappa_c = \left[\frac{\int_0^{\infty} \kappa^2 |\Psi(\kappa)|^2 d\kappa}{\int_0^{\infty} |\Psi(\kappa)|^2 d\kappa} \right]^{1/2}. \quad \text{(A2)}$$

We consider the Morelet wavelet for all transformations in this work:

$$\psi(x) = \frac{1}{\pi^{1/4}} \left(e^{i\kappa_c x} - e^{-\kappa_c^2/2} \right) e^{-x^2/2}. \quad \text{(A3)}$$
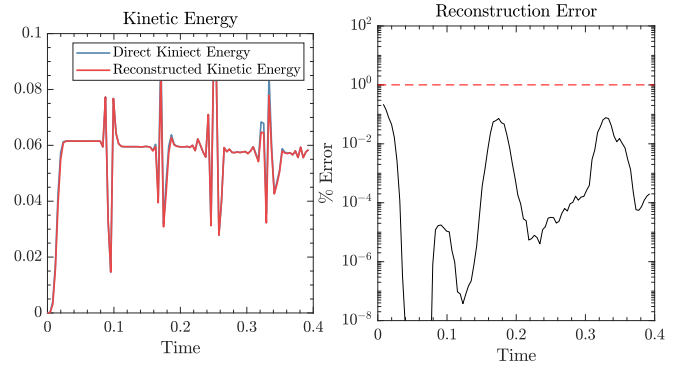

FIG. 11. The reconstructed kinetic energy and corresponding reconstruction error for the described wavelet partition scheme; red dashed line indicates 1% error.

For the scale and quantities of data sets considered in this work, computational efficiency is a requirement. To this end, the fast Fourier transform (FFT) is employed to speed up wavelet computations. Taking $\Psi(\kappa)$ as the analytical Fourier transform of the mother wavelet,

$$\Psi(\kappa) = e^{-(\kappa - \kappa_c)^2/2}, \quad \text{(A4)}$$

and $\tilde{x}(\kappa)$ the FFT of the signal, Parseval's theorem allows one to express wavelet transformation equivalently as

$$X(\kappa, x) = \sqrt{\frac{\kappa_c}{\kappa}} \int_{-\infty}^{\infty} \tilde{x}(\eta) \Psi^*(\eta \kappa / \kappa_c) e^{i\eta x} d\eta. \quad \text{(A5)}$$

Each wavelet transformation can be partitioned over space and wave number. The spectral partitions are defined over 12 regions spanning between $\kappa = 0$ and $\kappa = \pi$ to account for 12 different wavelet-domain representations of the spatial signal at each time instant. The kth wave number partition is defined as

$$X_k(\kappa, x) = X(\kappa, x) h_k(\kappa),$$
$$h_k(\kappa) = H \left(\kappa - \frac{(k-1)\pi}{12} \right) - H \left(\kappa - \frac{k\pi}{12} \right). \quad \text{(A6)}$$

The inverse wavelet transformation can be applied at each time snapshot to each wave number partition, $u_k(x) = \mathcal{W}^{-1}\{X_k(\kappa, x)\}$, which is computed as

$$u_k(x) = \frac{\sqrt{\kappa}}{\kappa_c^{3/2} C} \int_0^{\infty} \int_{-\infty}^{\infty} \hat{X}_k(\kappa, \xi) \Psi \left(\frac{\xi \kappa}{\kappa_c} \right) d\xi \, d\kappa, \quad \text{(A7)}$$

where $\hat{X}_k(\kappa, \xi)$ is the Fourier transformation of $X_k(\kappa, x)$ with respect to x. Figure 11 depicts the reconstructed kinetic energy of the lattice, KE_{rec}, as well as the directly computed (exact) kinetic energy from the numerical simulations, KE_{phys}, with the error between the two quantities computed by

$$e(t) = \frac{||KE_{\text{rec}}(t) - KE_{\text{phys}}(T)||}{||KE_{\text{phys}}(t)||}. \quad \text{(A8)}$$

2. Spectral entropy

Here, we provide more details pertaining to the spectral entropy plots displayed in Fig. 4. Figure 12 depicts the distribution of entropy using Eq. (3) to recover $H(x)$ for each t. The resulting matrix $\mathcal{H}(x, t)$ is plotted as an image for
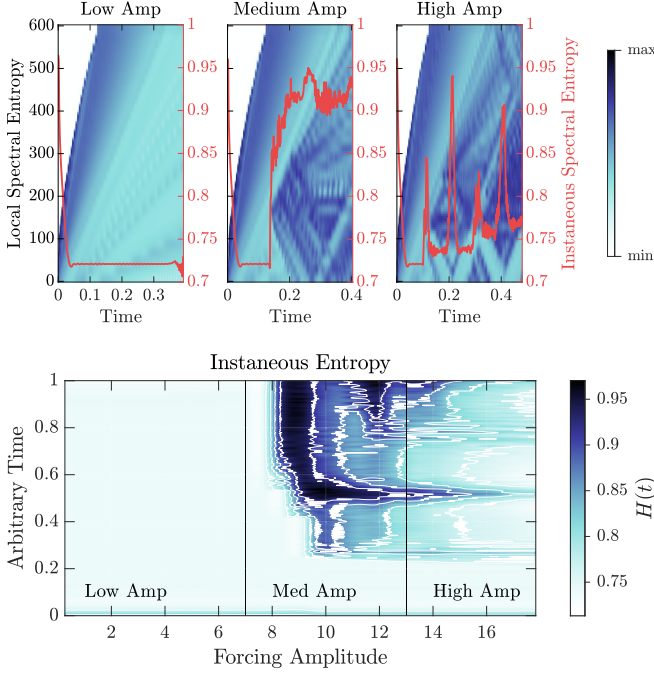
FIG. 12. Contours of the instantaneous wave number entropy across the time-entropy domain for low-, medium-, and high-amplitude simulations (top), and the summary contours of the instantaneous entropy $H(t)$ (bottom).

low, medium, and high excitation amplitudes. The distribution of high-entropy regions is clearly seen in the medium- and high-excitation-amplitude simulations as the VIs engage the incoming wave. Superimposed on each image is the *instantaneous* spectral entropy, which summarizes $\mathcal{H}(x, t)$ over space to render time-dependent measures $H(t)$.

A data set storing $H(t)$ for each excitation amplitude in the simulation ensemble can then be generated and plotted in the form of an image to study how the wave number entropy varies in time with respect to the forcing amplitude for a given lattice configuration. This is depicted in the bottom plot of Fig. 12. In the low-amplitude region with no VI engagement, no entropy is generated after excitation (as expected). For medium amplitudes, regions of *sustained* high wave number entropy are realized after the VIs engage the incident wave. In contrast, only *localized* patches of high entropy are seen for high-amplitude simulations, indicating that the VIs do not affect the global wave number of the lattice after the incident wave passes through (or reflects off of) the unit cells with embedded VIs.

3. Computing energy on each band

The computation of wave energy over each band in Sec. III is performed as follows. The data matrix for a given simulation is mapped to the Fourier domain using the 2D FFT algorithm $\mathcal{D}(\kappa, \omega) = \mathcal{F}^{x,t}\{\mathbf{u}(x, t)\}$. Next, frequency filters are constructed as follows:

$$G_k(\kappa, \omega) = \begin{cases} 1, & \omega \in \mathcal{B}_k, \ -\pi \leqslant \kappa \leqslant \pi \\ 0 & \text{otherwise,} \end{cases} \quad \text{(A9)}$$
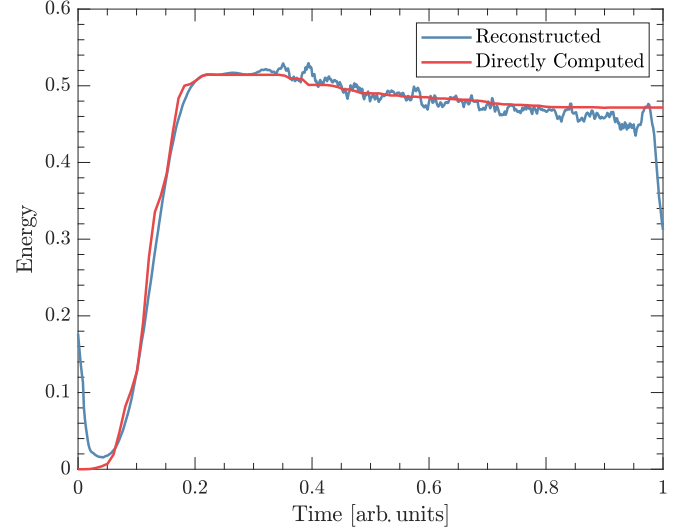

FIG. 13. Energy reconstruction of band-partitioning decomposition.

where the first four ranges of frequencies $\mathcal{B}_k$ are defined over the temporal frequency limits of the four pass-bands (PBs),

$$\mathcal{B}_1 = \min(\text{PB}_1) \leqslant \omega \leqslant \max(\text{PB}_1),$$
$$\mathcal{B}_2 = \min(\text{PB}_2) \leqslant \omega \leqslant \max(\text{PB}_2),$$
$$\mathcal{B}_3 = \min(\text{PB}_3) \leqslant \omega \leqslant \max(\text{PB}_3),$$
$$\mathcal{B}_4 = \min(\text{PB}_4) \leqslant \omega \leqslant \max(\text{PB}_4). \quad \text{(A10)}$$

The remaining two filter banks are constructed for the band gap between the acoustic band and first optical band (BG$_1$), and for the band gap between the upper two optical bands (BG$_2$):

$$\mathcal{B}_5 = \min(\text{BG}_1) \leqslant \omega \leqslant \max(\text{BG}_1),$$
$$\mathcal{B}_6 = \min(\text{BG}_2) \leqslant \omega \leqslant \max(\text{BG}_2). \quad \text{(A11)}$$

The spatial-temporal dynamics corresponding to each pass band and band-gap region are then given as

$$\mathbf{u}_k(x, t) = \mathcal{F}^{-x,-t}\{G_k(\kappa, \omega) \cdot \mathcal{D}(\kappa, \omega)\},$$

where $\mathcal{F}^{-x,-t}\{\}$ indicates the 2D inverse FFT with respect to x and t. The rigid boundaries of the filters in Fourier space inevitably result in minute numerical artifacts in the inverse transformation for each partition taking the form of ripples along the space-time boundaries. However, Fig. 13 shows that the reconstruction of energies computed by summing the energy over each band nearly identically to the energies computed for the direct numerical simulations, and hence these numerical artifacts are negligible.

APPENDIX B: NONLINEAR NORMAL MODE COMPUTATIONS

The recipe for NNM calculations follows very closely to the procedure outlined in [71]. For all FEP calculations, the shooting method used a prescribed initial step size of 1^{-5} and a tolerance of $\varepsilon = 1 \times 10^{-6}$. For low-energy orbits, Newmark integration was employed with 2000 steps per period, and Jacobian calculations of predictor-corrector steps

were computed using the sensitivity analysis in [71]. In region II, the unstable dynamics proved to be challenging for the computation of the corresponding NNM branch. Hence, sufficiently small predictor steps were required for convergence, with the residual reduction being varied from 10^{-12} to 10^{-10}. Sensitivity analysis was employed again to compute Jacobian terms in region II.

Once the dynamics of the NNMs stabilized to that of a definitive VI oscillator in region III, and moreover to smoothly stable NNMs in region IV, the finite-difference method sufficiently approximated Jacobian terms allowing for the implementation of fast and accurate Runge-Kutta-based methods such as ODE78. The nonsmooth nature of dynamics in region III would require still a great number of Newmark iterations to achieve the same accuracy as the ODE78 routine, and therefore the transition was made to a finite-difference Jacobian calculation scheme based on ODE78 for energies beyond region II to increase computational speed and reduce the number of steps required to resolve the high-energy regions of the FEP branch.

[1] S. A. Cummer, J. Christensen, and A. Alù, Controlling sound with acoustic metamaterials, Nat. Rev. Mater. **1**, 16001 (2016).

[2] J. U. Surjadi, L. Gao, H. Du, X. Li, X. Xiong, N. X. Fang, and Y. Lu, Mechanical metamaterials and their engineering applications, Adv. Eng. Mater. **21**, 1800864 (2019).

[3] M. I. Hussein, M. J. Leamy, and M. Ruzzene, Dynamics of phononic materials and structures: Historical origins, recent progress, and future outlook, Appl. Mech. Rev. **66**, 040802 (2014).

[4] S. Tol, F. Degertekin, and A. Erturk, 3D-printed phononic crystal lens for elastic wave focusing and energy harvesting, Addit. Manuf. **29**, 100780 (2019).

[5] K. K. Reichl and D. J. Inman, Lumped mass model of a 1D metastructure for vibration suppression with no additional mass, J. Sound Vib. **403**, 75 (2017).

[6] K. H. Matlack, A. Bauhofer, S. Krödel, A. Palermo, and C. Daraio, Composite 3D-printed metastructures for low-frequency and broadband vibration absorption, Proc. Natl. Acad. Sci. USA **113**, 8386 (2016).

[7] J. Mueller, K. H. Matlack, K. Shea, and C. Daraio, Energy absorption properties of periodic and stochastic 3D lattice materials, Adv. Theory Simul. **2**, 1900081 (2019).

[8] L. Sirota, D. Sabsovich, Y. Lahini, R. Ilan, and Y. Shokef, Real-time steering of curved sound beams in a feedback-based topological acoustic metamaterial, Mech. Syst. Signal Process. **153**, 107479 (2021).

[9] R. K. Pal and M. Ruzzene, Edge waves in plates with resonators: An elastic analogue of the quantum valley Hall effect, New J. Phys. **19**, 025001 (2017).

[10] H. Chen, H. Nassar, and G. Huang, A study of topological effects in 1D and 2D mechanical lattices, J. Mech. Phys. Solids **117**, 22 (2018).

[11] J. R. Tempelman, A. F. Vakakis, and K. H. Matlack, A modal decomposition approach to topological wave propagation, J. Sound Vib. **568**, 118033 (2024).

[12] G. U. Patil and K. H. Matlack, Review of exploiting nonlinearity in phononic materials to enable nonlinear wave responses, Acta Mech. **233**, 1 (2022).

[13] J. O. Vasseur, O. B. Matar, J. F. Robillard, A.-C. Hladky-Hennion, and P. A. Deymier, Band structures tunability of bulk 2D phononic crystals made of magneto-elastic materials, AIP Adv. **1**, 041904 (2011).

[14] F. Allein, V. Tournat, V. E. Gusev, and G. Theocharis, Tunable magneto-granular phononic crystals, Appl. Phys. Lett. **108**, 161903 (2016).

[15] C. D. Pierce, C. L. Willey, V. W. Chen, J. O. Hardin, J. D. Berrigan, A. T. Juhl, and K. H. Matlack, Adaptive elastic metastructures from magneto-active elastomers, Smart Mater. Struct. **29**, 065004 (2020).

[16] Y. Cheng, X. J. Liu, and D. J. Wu, Temperature effects on the band gaps of Lamb waves in a one-dimensional phononic-crystal plate (L), J. Acoust. Soc. Am. **129**, 1157 (2011).

[17] Y. Yao, F. Wu, X. Zhang, and Z. Hou, Thermal tuning of Lamb wave band structure in a two-dimensional phononic crystal plate, J. Appl. Phys. **110**, 123503 (2011).

[18] Z. Zhao, X. Cui, Y. Yin, Y. Li, and M. Li, Thermal tuning of vibration band gaps in homogenous metamaterial plate, Int. J. Mech. Sci. **225**, 107374 (2022).

[19] *Nonlinearities in Periodic Structures and Metamaterials*, edited by C. Denz, S. Flach, and Y. S. Kivshar (Springer, Berlin, 2010).

[20] F. Li, D. Ngo, J. Yang, and C. Daraio, Tunable phononic crystals based on cylindrical Hertzian contact, Appl. Phys. Lett. **101**, 171903 (2012).

[21] R. Chaunsali, F. Li, and J. Yang, Stress wave isolation by purely mechanical topological phononic crystals, Sci. Rep. **6**, 30662 (2016).

[22] R. Chaunsali, E. Kim, A. Thakkar, P. G. Kevrekidis, and J. Yang, Demonstrating an *in situ* topological band transition in cylindrical granular chains, Phys. Rev. Lett. **119**, 024301 (2017).

[23] R. K. Narisetti, M. J. Leamy, and M. Ruzzene, A perturbation approach for predicting wave propagation in one-dimensional nonlinear periodic structures, J. Vib. Acoust. **132**, 031001 (2010).

[24] J. R. Tempelman, K. H. Matlack, and A. F. Vakakis, Topological protection in a strongly nonlinear interface lattice, Phys. Rev. B **104**, 174306 (2021).

[25] K. R. Jayaprakash, Y. Starosvetsky, A. F. Vakakis, M. Peeters, and G. Kerschen, Nonlinear normal modes and band zones in granular chains with no pre-compression, Nonlinear Dyn. **63**, 359 (2011).

[26] A. Mojahed and A. F. Vakakis, Certain aspects of the acoustics of a strongly nonlinear discrete lattice, Nonlinear Dyn. **99**, 643 (2020).

[27] O. V. Gendelman and A. F. Vakakis, Introduction to a topical issue "nonlinear energy transfer in dynamical and acoustical systems", Philos. Trans. R. Soc. A **376**, 20170129 (2018).

[28] V. Rothos and A. Vakakis, Dynamic interactions of traveling waves propagating in a linear chain with an local essentially nonlinear attachment, Wave Motion **46**, 174 (2009).

[29] A. F. Vakakis, M. A. AL-Shudeifat, and M. A. Hasan, Interactions of propagating waves in a one-dimensional chain of linear oscillators with a strongly nonlinear local attachment, Meccanica **49**, 2375 (2014).

[30] H. Nassar, B. Yousefzadeh, R. Fleury, M. Ruzzene, A. Alù, C. Daraio, A. N. Norris, G. Huang, and M. R. Haberman, Nonreciprocity in acoustic and elastic materials, Nat. Rev. Mater. **5**, 667 (2020).

[31] J. Bunyan, K. J. Moore, A. Mojahed, M. D. Fronk, M. Leamy, S. Tawfick, and A. F. Vakakis, Acoustic nonreciprocity in a lattice incorporating nonlinearity, asymmetry, and internal scale hierarchy: Experimental study, Phys. Rev. E **97**, 052211 (2018).

[32] M. D. Fronk, S. Tawfick, C. Daraio, S. Li, A. Vakakis, and M. J. Leamy, Acoustic non-reciprocity in lattices with nonlinearity, internal hierarchy, and asymmetry: Computational study, J. Vib. Acoust. **141**, 051011 (2019).

[33] I. Grinberg, A. F. Vakakis, and O. V. Gendelman, Acoustic diode: Wave non-reciprocity in nonlinearly coupled waveguides, Wave Motion **83**, 49 (2018).

[34] C. Fu, B. Wang, T. Zhao, and C. Q. Chen, High efficiency and broadband acoustic diodes, Appl. Phys. Lett. **112**, 051902 (2018).

[35] A. Darabi, L. Fang, A. Mojahed, M. D. Fronk, A. F. Vakakis, and M. J. Leamy, Broadband passive nonlinear acoustic diode, Phys. Rev. B **99**, 214305 (2019).

[36] T. Devaux, A. Cebrecos, O. Richoux, V. Pagneux, and V. Tournat, Acoustic radiation pressure for nonreciprocal transmission and switch effects, Nat. Commun. **10**, 3292 (2019).

[37] N. Mork, M. D. Fronk, M. B. Sinclair, and M. J. Leamy, Nonlinear hierarchical unit cell for passive, amplitude-dependent filtering of acoustic waves, Extreme Mech. Lett. **57**, 101915 (2022).

[38] R. W. Boyd, *Nonlinear Optics* (Academic Press, San Diego, 1992), p. 439.

[39] A. F. Vakakis, O. V. Gendelman, L. A. Bergman, A. Mojahed, and M. Gzal, Nonlinear targeted energy transfer: State of the art and new perspectives, Nonlinear Dyn. **108**, 711 (2022).

[40] A. F. Vakakis, O. V. Gendelman, L. A. Bergman, D. M. McFarland, and G. Kerschen, *Nonlinear Targeted Energy Transfer in Mechanical and Structural Systems* (Springer, Berlin, 2008).

[41] G. Kopidakis, S. Aubry, and G. P. Tsironis, Targeted energy transfer through discrete breathers in nonlinear systems, Phys. Rev. Lett. **87**, 165501 (2001).

[42] J. Wang, N. Wierschem, B. F. Spencer, and X. Lu, Numerical and experimental study of the performance of a single-sided vibro-impact track nonlinear energy sink, Earthquake Eng. Struct. Dyn. **45**, 635 (2015).

[43] A. F. Vakakis and O. Gendelman, Energy pumping in nonlinear mechanical oscillators: Part II—resonance capture, J. Appl. Mech. **68**, 42 (2001).

[44] A. F. Vakakis, Inducing passive nonlinear energy sinks in vibrating systems, J. Vib. Acoust. **123**, 324 (2001).

[45] M. Taleshi, M. Dardel, and M. H. Pashaie, Passive targeted energy transfer in the steady state dynamics of a nonlinear plate with nonlinear absorber, Chaos Solitons Fractals **92**, 56 (2016).

[46] Y. Starosvetsky and O. V. Gendelman, Attractors of harmonically forced linear oscillator with attached nonlinear energy sink. II: Optimization of a nonlinear vibration absorber, Nonlinear Dyn. **51**, 47 (2007).

[47] Y. Starosvetsky and O. Gendelman, Interaction of nonlinear energy sink with a two degrees of freedom linear system: Internal resonance, J. Sound Vib. **329**, 1836 (2010).

[48] D. Qiu, S. Seguy, and M. Paredes, Tuned nonlinear energy sink with conical spring: Design theory and sensitivity analysis, J. Mech. Des. **140**, 011404 (2017).

[49] D. Huang, R. Li, and G. Yang, On the dynamic response regimes of a viscoelastic isolation system integrated with a nonlinear energy sink, Commun. Nonlinear Sci. Numer. Simul. **79**, 104916 (2019).

[50] F. Georgiades and A. Vakakis, Dynamics of a linear beam with an attached local nonlinear energy sink, Commun. Nonlinear Sci. Numer. Simul. **12**, 643 (2007).

[51] O. Gendelman, L. I. Manevitch, A. F. Vakakis, and R. M'Closkey, Energy pumping in nonlinear mechanical oscillators: Part I—dynamics of the underlying Hamiltonian systems, J. Appl. Mech. **68**, 34 (2001).

[52] O. V. Gendelman, Transition of energy to a nonlinear localized mode in a highly asymmetric system of two oscillators, Nonlinear Dyn. **25**, 237 (2001).

[53] O. V. Gendelman, Y. Starosvetsky, and M. Feldman, Attractors of harmonically forced linear oscillator with attached nonlinear energy sink I: Description of response regimes, Nonlinear Dyn. **51**, 31 (2007).

[54] A. Darabi and M. J. Leamy, Clearance-type nonlinear energy sinks for enhancing performance in electroacoustic wave energy harvesting, Nonlinear Dyn. **87**, 2127 (2017).

[55] H. Dai, A. Abdelkefi, and L. Wang, Vortex-induced vibrations mitigation through a nonlinear energy sink, Commun. Nonlinear Sci. Numer. Simul. **42**, 22 (2017).

[56] L. A. Bergman, O. V. Gendelman, G. Kerschen, Y. S. Lee, and D. M. McFarland, *Nonlinear Targeted Energy Transfer in Mechanical and Structural Systems* (Springer-Verlag GmbH, Berlin, 2008).

[57] L. I. Manevitch, A concept of limiting phase trajectories and description of highly non-stationary resonance processes, Appl. Math. Sci. **9**, 4269 (2015).

[58] F. Nucera, A. F. Vakakis, D. M. McFarland, L. A. Bergman, and G. Kerschen, Targeted energy transfers in vibro-impact oscillators for seismic mitigation, Nonlinear Dyn. **50**, 651 (2007).

[59] O. Gendelman, Analytic treatment of a system with a vibro-impact nonlinear energy sink, J. Sound Vib. **331**, 4599 (2012).

[60] T. Li, S. Seguy, and A. Berlioz, Optimization mechanism of targeted energy transfer with vibro-impact energy sink under periodic and transient excitation, Nonlinear Dyn. **87**, 2415 (2017).

[61] M. Gzal, B. Fang, A. F. Vakakis, L. A. Bergman, and O. V. Gendelman, Rapid non-resonant intermodal targeted energy transfer (IMTET) caused by vibro-impact nonlinearity, Nonlinear Dyn. **101**, 2087 (2020).

[62] M. Gzal, A. F. Vakakis, L. A. Bergman, and O. V. Gendelman, Extreme intermodal energy transfers through vibro-impacts for highly effective and rapid blast mitigation, Commun. Nonlinear Sci. Numer. Simul. **103**, 106012 (2021).

[63] J. R. Tempelman, A. Mojahed, M. Gzal, K. H. Matlack, O. V. Gendelman, L. A. Bergman, and A. F. Vakakis, Experimental inter-modal targeted energy transfer in a cantilever beam undergoing vibro-impacts, J. Sound Vib. **539**, 117212 (2022).

[64] K. H. Hunt and F. R. E. Crossley, Coefficient of restitution interpreted as damping in vibroimpact, J. Appl. Mech. **42**, 440 (1975).

[65] A. Mojahed, L. A. Bergman, and A. F. Vakakis, New inverse wavelet transform method with broad application

in dynamics, Mech. Syst. Signal Process. **156**, 107691 (2021).

[66] B. Boashash, *Time-Frequency Signal Analysis and Processing: A Comprehensive Review* (Academic Press, San Diego, 2013).

[67] See Supplemental Material at http://link.aps.org/supplemental/10.1103/PhysRevE.108.044214 for additional results and details.

[68] A. F. Vakakis, L. I. Manevitch, Y. V. Mikhlin, V. N. Pilipchuk, and A. A. Zevin, *Normal Modes and Localization in Nonlinear Systems* (Wiley, New York, 2008), p. 552.

[69] G. Kerschen, M. Peeters, J. Golinval, and A. Vakakis, Nonlinear normal modes, part I: A useful framework for the structural dynamicist, Mech. Syst. Signal Process. **23**, 170 (2009).

[70] K. V. Avramov and Y. V. Mikhlin, Review of applications of nonlinear normal modes for vibrating mechanical systems, Appl. Mech. Rev. **65**, 020801 (2013).

[71] M. Peeters, R. Viguié, G. Sérandour, G. Kerschen, and J.-C. Golinval, Nonlinear normal modes, part II: Toward a practical computation using numerical continuation techniques, Mech. Syst. Signal Process. **23**, 195 (2009).

[72] Y. S. Lee, F. Nucera, A. F. Vakakis, D. M. McFarland, and L. A. Bergman, Periodic orbits, damped transitions and targeted energy transfers in oscillators with vibro-impact attachments, Physica D **238**, 1868 (2009).

[73] H. Tao and J. Gibert, Periodic orbits of a conservative 2-DOF vibro-impact system by piecewise continuation: Bifurcations and fractals, Nonlinear Dyn. **95**, 2963 (2019).

[74] E. Moussi, S. Bellizzi, B. Cochelin, and I. Nistor, Nonlinear normal modes of a two degrees-of-freedom piecewise linear system, Mech. Syst. Signal Process. **64–65**, 266 (2015).